

---

# Improved Convex Decomposition with Ensembling and Boolean Primitives

---

Vaibhav Vavilala  
UIUC

Florian Kluger  
Leibniz Universität Hannover

Seemantihar Jain  
UIUC

Bodo Rosenhahn  
Leibniz Universität Hannover

Anand Bhattad  
TTIC

David Forsyth  
UIUC

## Abstract

Describing a scene in terms of primitives – geometrically simple shapes that offer a parsimonious but accurate abstraction of structure – is an established and difficult fitting problem. Different scenes require different numbers of primitives, and these primitives interact strongly. Existing methods are evaluated by predicting depth, normals and segmentation from the primitives, then evaluating the accuracy of those predictions. The state of the art method involves a learned regression procedure to predict a start point consisting of a fixed number of primitives, followed by a descent method to refine the geometry and remove redundant primitives.

CSG (Constructive Solid Geometry) representations are significantly enhanced by a set-differencing operation. Our representation incorporates *negative* primitives, which are differenced from the positive primitives. These notably enrich the geometry that the model can encode, while complicating the fitting problem. This paper demonstrates a method that can (a) incorporate these negative primitives and (b) choose the overall number of positive and negative primitives by ensembling. Extensive experiments on the standard NYUv2 dataset confirm that (a) this approach results in substantial improvements in depth representation and segmentation over SOTA and (b) negative primitives make a notable contribution to accuracy. Our method is robustly applicable across datasets: in a first, we evaluate primitive prediction for LAION images.

## 1 Introduction

Geometric representations of scenes and objects as *primitives* – simple geometries that expose structure while suppressing detail – should allow simpler, more general reasoning. It is easier to plan moving a cuboid through stylized free space than moving a specific chair through a particular living room. As another example, an effective primitive representation should simplify selecting and manipulating objects in scenes as in image-based scene editing [3, 61]. But obtaining primitive representations that abstract usefully and accurately has been hard (review Sec. 2).

Primitive prediction methods for objects are well established (Sec. 2), but are rare for scenes. There are two main types of method. A **descent method** chooses primitives for a given geometry by minimizing a cost function. Important obstacles include: different geometries require different numbers of primitives; the choice of primitive appears to be important in ways that are opaque; the fitting problem has large numbers of local minima; and finding a good start point is difficult. In particular, incremental fitting procedures are traditionally defeated by interactions between primitives. Sec. 3.2 demonstrates an extremely strong and quite simple descent-based fitting baseline. A **regression method** uses a learned predictor to map geometry to primitives and their parameters.

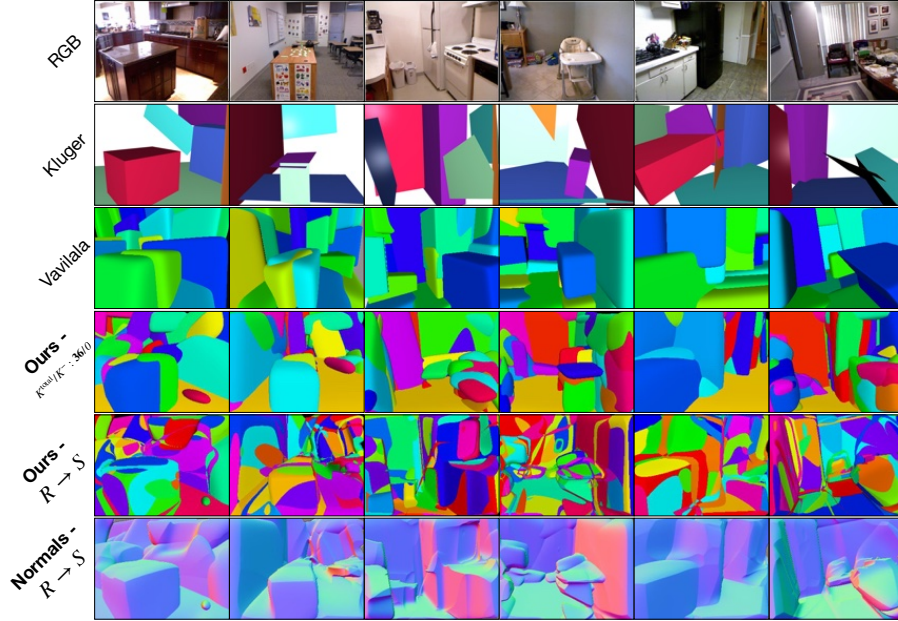


Figure 1: We present a method that advances the SOTA for primitive decomposition by using ensembling and boolean primitives. Prior art shown in 2<sup>nd</sup> row [28] and 3<sup>rd</sup> row [60] for comparison. (4<sup>th</sup> row) We show results from our approach with 36 primitives, none boolean. Our procedure encodes geometry quite closely. (5<sup>th</sup> and 6<sup>th</sup> row) With boolean primitives, we can encode a rich arrangement of shapes. Here, we ensemble many predictors and show the best one. In these six cases, a model with boolean primitives was chosen. The normals make it clear that boolean primitives are scooping geometry away from positive primitives.

These methods can pool examples to avoid local minima, but may not get the best prediction for a given input. The SOTA method [60] for parsing indoor scenes uses a regression method to predict a start point consisting of a fixed set of primitives, followed by polishing and pruning.

For **negative primitives**, the predicted geometry is the regularized set difference between the union of positive primitives and the union of negative primitives [46, 47]. Admitting negative primitives significantly enriches the range of geometries that can be encoded (Sec. 3). This paper shows two procedures that yield significant (over 50% relative error) improvements in accuracy. First, we allow a small number of *negative* primitives in the sense of constructive solid geometry (CSG). Second, we show that selecting the number of primitives per scene (using an appropriately constructed ensembling method) produces very strong improvements in accuracy at small cost in inference time. Even without ensembling and boolean primitives, our primitive decomposition pipeline yields drastic improvements over prior work in geometric and segmentation accuracy. Our contributions are:

**Fitting CSG models to in the wild images:** We believe there is no other method that can fit CSG models including a set differencing operator to in-the-wild images of scenes. We demonstrate qualitative and quantitative benefits to fitting models with negative primitives.

**Test-time ensembling:** Primitive decomposition is unusual, in that one can evaluate a predicted solution at test time without ground truth primitive data by comparing to a depth prediction. We show we can search efficiently for the right number of positive and negative primitives for each scene. The resulting estimate is better than any obtained using a fixed number of positives and negatives.

**Accuracy:** Our method outperforms all available baselines and SOTA on NYUv2, and we demonstrate that it produces accurate representations of diverse scenes from LAION.

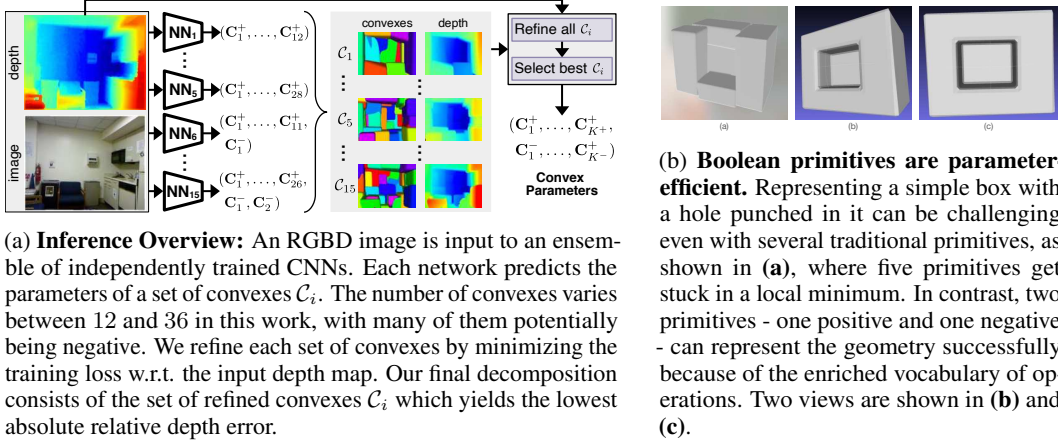


Figure 2: Overview of our approach (left) and demonstration of boolean primitives (right).

## 2 Related Work

Primitives date to the origins of computer vision. Roberts worked with blocks [49]; Binford with generalized cylinders [5]; Biederman with geons [4]. Ideally, complex objects might be handled with simple primitives [7] where each primitive is a semantic part [4, 5, 59]. Primitives can be recovered from image data [39, 51], and allow simplified geometric reasoning [42].

For individual objects, neural methods could predict the right set of primitives by predicting solutions for test data that are “like” those that worked for training data. Tulsiani *et al.* parse 3D shapes into cuboids, trained without ground truth segmentations [57]. Zou *et al.* parse with a recurrent architecture [70]. Liu *et al.* produce detailed reconstructions of objects in indoor scenes, but do not attempt parsimonious abstraction [33]. Worryingly, 3D reconstruction networks might rely on object semantics [55]. Deng *et al.* (CVXNet) represent objects as a union of convexes, again training without ground truth segmentations [9]. An early variant of CVXNet can recover 3D representations of poses from single images, with reasonable parses into parts [8]. Meshes can be decomposed into near convex primitives, by a form of search [63]. Part decompositions have attractive editability [19]. Regression methods face some difficulty producing different numbers of primitives per scene (CVXNet uses a fixed number; [57] predicts the probability a primitive is present; one also might use Gumbel softmax [23]). Primitives that have been explored include: cuboids [6, 13, 36, 57, 48, 52, 54, 28]; superquadrics [2, 22, 40]; planes [7, 31]; and generalized cylinders [39, 68, 30]. There is a recent review in [12].

Neural Parts [41] decomposes an object given by an image into a set of non-convex shapes. CAPRI-Net [67] decomposes 3D objects given as point clouds or voxel grids into assemblies of quadric surfaces. DeepCAD [64] decomposes an object into a sequence of commands describing a CAD model, but requires appropriately annotated data for training. Point2Cyl [58] is similar, but predicts the 2D shapes as an SDF. Notably, [67, 64, 58] also utilise CSG with negative parts but, unlike our work, focus on CAD models of single objects instead of complex real-world scenes.

Hoiem *et al* parse outdoor scenes into vertical and horizontal surfaces [21, 20]; Gupta *et al* demonstrate a parse into blocks [14]. Indoor scenes can be parsed into: a cuboid [16, 60]; beds and some furniture as boxes [18]; free space [17]; and plane layouts [53, 32]. If RGBD is available, one can recover layout in detail [69]. Patch-like primitives can be imputed from data [11]. Jiang demonstrates parsing RGBD images into primitives by solving a 0-1 quadratic program [24]. Like that work, we evaluate segmentation by primitives (see [24], p. 12), but we use original NYUv2 labels instead of the drastically simplified ones in the prior work. Also, our primitives are truly convex. Monnier *et al* and Alaniz *et al* decompose scenes into sets of superquadrics using differentiable rendering, which requires calibrated multi-view images as input [37, 1]. Most similar to our work is that of Kluger *et al*, who identify cuboids sequentially with a RANSAC-like greedy algorithm [10, 27, 28, 29, 26].

The success of a descent method depends critically on the start point, typically dealt with using greedy algorithms (rooted in RANSAC [10]; note the prevalence of RANSAC in a recent review [25]);

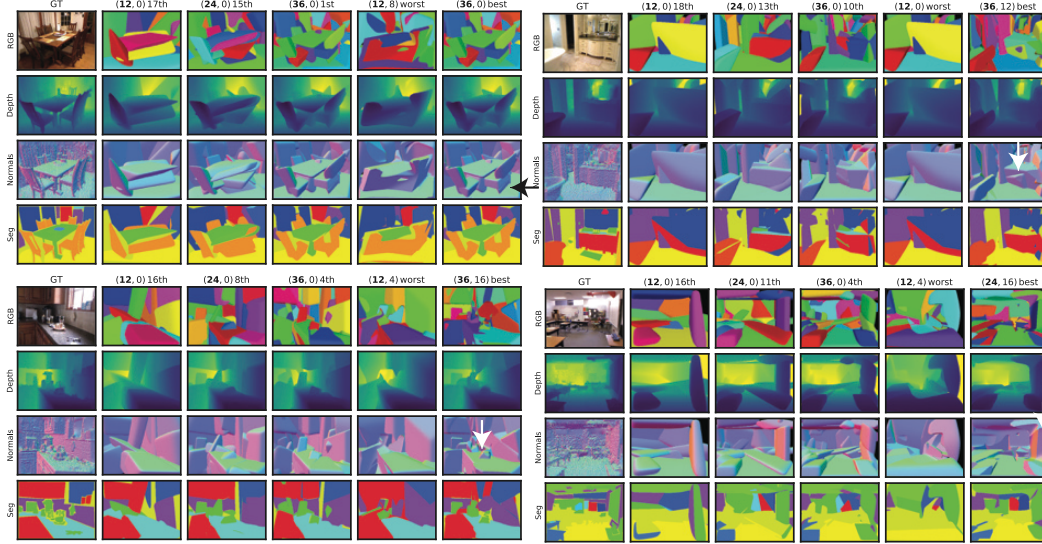


Figure 3: Visualizations of various primitive predictions for four scenes from NYUv2. We show ground truth (first column in each block); predictions of  $(12, 0)$ ,  $(24, 0)$  and  $(36, 0)$  models; the prediction of the model that made the *worst* prediction for the scene; and the prediction of the model that made the *best* prediction. The best choice of primitive counts  $K^{total}$  varies from scene to scene. Notice some complex objects made up as composites of positive primitives (black arrow) and negative primitives “carving out” shapes. The segmentation label is the oracle label described in the text.

randomized search [43, 15]; or multiple starts. Remarkably, as Sec. 3.2 shows, modern first-order methods (we used AdamW [34]) are capable of producing fairly good primitive representations from a random start point.

### 3 Method

*At inference time*, one can evaluate a predicted solution by comparing the primitive predicted depth with a depth map predicted from an image. In turn, one can polish a representation predicted by a network, and choose between representations. Write  $K^{total}$  for the total number of primitives and  $K^-$  for the number of negatives to be predicted. For each  $(K^{total}, K^-)$  we wish to investigate, we train a prediction network. Then, at inference time, we produce a set of primitives from each network, polish it, select the primitives with the best loss and report that, so different scenes will have predictions involving different numbers of primitives. Our approach is a generalization of the architecture of [60], but produces very significant improvements in performance (Sec. 4). Negative primitives require some minor modifications of their procedure (Sec. 3) We use their losses with some omissions (Sec. 3.1). Our polishing procedure is somewhat different (Sec. 3.2).

Our network requires RGBD input. If depth measurements are not available, our method works well with single image depth predictors. Our losses require a point cloud that is extracted from the depth image via the heuristic described in [60]. Our method works both when GT depth is and is not available, as we can use pretrained networks [45, 65] to obtain inferred depth maps. Fig. 2a provides an overview of our inference pipeline.

**Base primitives:** Our primitives are smoothed polytopes as described in [9]. For 6-faced parallelepipeds, each primitive is parametrized by a center (3 DOF’s), 3 normals (6 DOF’s), 6 offsets (6 DOF’s) and a blending term (1 DOF). The blended half-plane approach eases training and also enables fitting curved surfaces. We fit 6-faced parallelepipeds for fair comparative evaluation, and then show that more faces per polytope yields better representations (see Table 6 in supplementary).

**Negative primitives:** Set differencing produces a notably more complex geometric representation. Assume we have  $K^{total}$  primitives of which  $K^-$  are negative, each with  $f$  faces. Label an image pixel by the face intersection that produced that pixel (as in our face segmentation figures, e.g. Fig. 4).



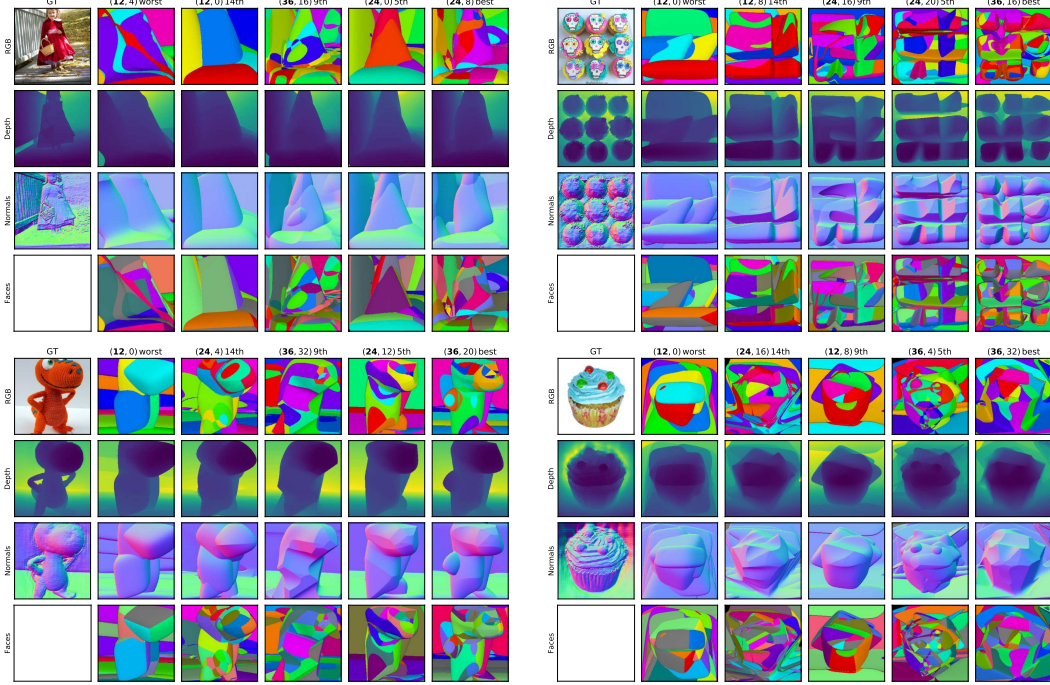


Figure 4: Visualizations of various primitive predictions for four scenes from LAION. We show ground truth (first column in each block); the prediction of the model that made the *worst* prediction for the scene; the prediction of the model that made the *best* prediction rightmost; and in-between results shown in intermediate columns. While our models produce good fits on average, ensembling helps select the optimal primitive count for each test scene and avoids poor solutions. The best choice of primitive counts  $K^{total}$  varies from scene to scene. **Bottom row** in each block shows face labels – no oracle segmentation is available. Note how primitives can follow complex structures; how they tend to “stick” to object properties; and how the number of face labels grows very quickly with the number of negative primitives. See Figs. 9 and 10 for additional examples.

Generic pixels could result from either ray intersection with a face of a positive primitive or with a face of a negative primitive inside some positive. This argument means that there are a maximum of  $f \times (K^{total} - K^-) \times (1 + K^-)$  pixel labels; note how this number grows very quickly with an increase in the number of negative primitives, an effect that can be seen in Fig. 4. Negative primitives are easily handled with indicator functions. We define the indicator for a set of primitives  $O : \mathbb{R}^3 \rightarrow [0, 1]$ , with  $O(x) = 0$  indicating free space, and  $O(x) = 1$  indicating a query point  $x \in \mathbb{R}^3$  is inside the volume. Write  $O^+(x)$  for the indicator function for the set of positive primitives,  $O^-(x)$  for negative primitives. The indicator for our representation is then:

$$O(x) = \text{relu}(O^+(x) - O^-(x)). \quad (1)$$

### 3.1 Losses

Our modified representation allows re-using the existing sample loss and auxiliary losses (unique parametrization loss, overlap loss, guidance loss, localization loss) [9, 60] for both  $O^+(x)$  and  $O^-(x)$ . While a Manhattan World loss was found to be helpful for NYUv2, it hurt quality on general in-the-wild LAION images in our testing so we leave out that loss in this work. We do not consider the volume loss or segmentation loss from [60] in our experimentation, as they were shown to have an approximately neutral effect in the original paper.

| Method                      | $K^{total}$ | $K^-$ | AbsRel↓       | Normals Mean↓ | Normals Median↓ | SegAcc↑      | Time (s) | Mem (GB) |
|-----------------------------|-------------|-------|---------------|---------------|-----------------|--------------|----------|----------|
| 12                          | <b>12</b>   | 0     | 0.0622        | 34.4          | 26.3            | 0.651        | 0.84     | 3.53     |
| 24                          | <b>24</b>   | 0     | 0.052         | 33            | 25              | 0.7          | 1.46     | 5.57     |
| 36                          | <b>36</b>   | 0     | 0.0484        | 32.3          | 24.4            | 0.723        | 2.06     | 7.61     |
| best                        | <b>36</b>   | 12    | 0.0452        | 32.1          | 24              | <b>0.765</b> | 2.06     | 7.61     |
| pos $S \rightarrow R$       | <b>26.1</b> | 0     | 0.0527        | 33            | 24.9            | 0.7          | 2.08     | 7.61     |
| pos + neg $S \rightarrow R$ | <b>29</b>   | 10.4  | 0.0492        | 32.9          | 24.7            | 0.733        | 2.13     | 7.61     |
| pos $R \rightarrow S$       | <b>33.6</b> | 0     | 0.0476        | 32.3          | 24.4            | 0.72         | 4.37     | 7.61     |
| pos + neg $R \rightarrow S$ | <b>35</b>   | 14.7  | <b>0.0417</b> | <b>31.9</b>   | <b>24</b>       | 0.756        | 29.9     | 7.61     |
| Vavilala & Forsyth [60]     | <b>13.9</b> | 0     | 0.098         | 37.4          | 32.4            | 0.618        | 40       | 6.77     |

Table 1: Comparison to SOTA (last row) on NYUv2. **All rows except the last were trained using our procedure.** Our best approach (second last row) polishes then chooses from 18 different models with different numbers of primitives. Other rows show variants of our model. **First three rows:** we train a primitive generation model according to the procedure laid out in Sec 3, without boolean primitives. Next row: **36** total primitives with **12** negative was our best network as measured by AbsRel. **Next four rows** Ensembling strongly improves error metrics, particularly AbsRel. pos + neg refers to all 18 models available for ensembling, whereas pos refers to only 3 models without boolean primitives available.  $S \rightarrow R$  refers to only refining the output of the model with the best sample classification;  $R \rightarrow S$  means we finetune all models and pick the best one. In this table, we finetune assuming GT depth is available at test time, though our method still works even when depth is inferred by a pretrained depth estimator. The fact that substantial gains can be achieved from  $R \rightarrow S$  implies that the best start point may not yield the best end point – meaning the fitting problem is hard. Time and memory estimates are presented as well. **Last row:** we compare our methods against existing work. Any individual model we train obtains better error metrics with less compute. Timings for ensembling shows estimated total cost of running all the methods and selecting the best one; memory refers to peak GPU memory usage.

### 3.2 Polishing and Descent

Test-time finetuning is possible because we can evaluate the primitive prediction against the predicted depth map, then use the training losses at test-time. The fit is improved by using more 3D samples in these losses per image at test-time. Our polishing procedure has been heavily optimized.

In fact, our test-time refinement procedure is effective enough that we can fit a primitive representation *using only a random start*. We are aware of no other primitive fitting procedure that can operate with pure descent and no random restart or incremental process. This supplies an interesting baseline; Sec. 4 demonstrates that this baseline is highly inefficient compared to polishing a network prediction, and is not competitive in accuracy.

### 3.3 Choosing the Number of Primitives

Much of the literature on primitive decomposition fits a fixed number of primitives [9]. In contrast, we train 18 models for  $(K^{total}, K^-)$ , with  $K^{total} \in \{12, 24, 36\}$  and  $K^- \in \{0, 4, \dots, K^{total} - 4\}$ . We investigate two strategies for choosing the best prediction (and so the best set of primitives) for a given test image:  $S \rightarrow R$ , where we select the best neural prediction then refine it; and  $R \rightarrow S$ , where we refine all predictions then select the best.

### 3.4 Implementation Details

Our neural architecture is a ResNet-18 encoder (accepting RGBD input), followed by a decoder consisting of three linear layers of sizes [1048, 1048, 2048] and LeakyRelu activations. We do not freeze any layers during training. The dimensionality of the final output varies based on the number of primitives the model is trained to produce (as we train different models for different numbers of primitives in this work). We implement our procedure in PyTorch and train all networks with AdamW optimizer, learning rate  $2 \times 10^{-4}$ , batch size 96, mixed-precision training, for 20000 iterations, on a single A40 GPU. Each image is resized to  $240 \times 320$  resolution. Although we train at fixed resolution, our model can run inference at variable aspect ratio, as would be expected from CNNs like ResNet. It takes 39 mins to train a 12 primitive model and 62 mins to train a 36 primitive model. On LAION, we train at  $256 \times 256$  resolution. We use random flip, scale, and crop during training.

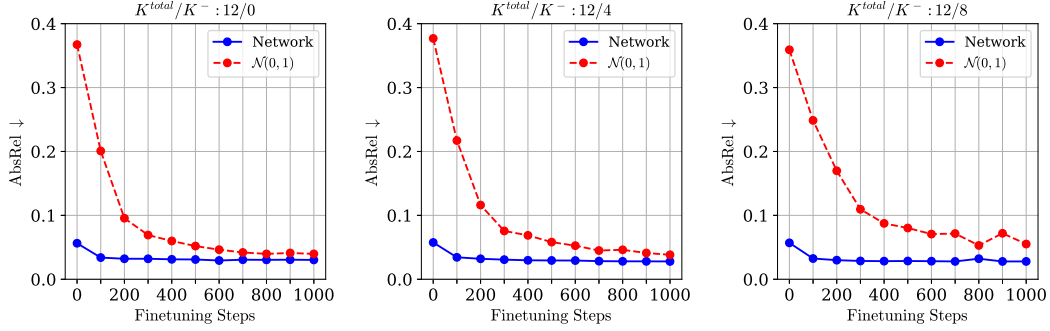


Figure 5: **Network start is beneficial.** Initializing our finetuning process with primitives predicted by our network (blue line) yields better primitives after finetuning than random start (red line). Inference from our network is around 0.0006 seconds per image, whereas 200 iterations of finetuning takes nearly .7 seconds when  $K^{total} = 12$ . In practice, network start saves around 900 FT steps and can achieve a better quality than random start. It also appears to be harder to fit negative primitives than positives (there is a greater gap in the final AbsRel between the two curves when there are negative primitives). Based on these results, we use 200 finetuning steps to balance compute and quality when reporting error metrics in this paper. Further, the fact that it is even possible to generate high-quality primitives via pure optimization, without a neural network, is new in the context of recent primitive-generation literature. Results shown on 100 random test images from LAION.

## 4 Results

Qualitative results appear in Fig 3 and Fig 4. Note how primitives can combine to form complex structures; how negative primitives “carve out” complex shapes; how primitives tend to “stick” to object properties (for example, heads; a house); and how the number of face labels grows very quickly with the number of negative primitives.

### 4.1 Evaluating a Primitive Representation

While *producing* a primitive representation has a long history ([35], Sec. 2), not much is known about how one is to be *used* apart from the original recognition argument, now clearly an anachronism. Recent work in conditioned image synthesis ([61, 3]) suggests that applications might need (a) a relatively compact representation (so that users can, say, move primitives around) and (b) one that accurately reflects depth, normals and (ideally) segmentation.

We compare primitive methods against one another using standard metrics for depth, normal and segmentation. Specialized predictors of depth, normal and segmentation outperform primitive methods on these metrics. But we would not use a primitive predictor to actually predict depth, normal or segmentation – instead, we are using the metrics to determine whether very highly simplified representations achieve reasonable accuracy. Our procedure uses the standard 795/654 train/test NYUv2 split [38]. We hold out 5% of training images for validation. We use this dataset primarily to maintain consistency in evaluating against prior art.

For NYUv2, we compare the depth map predicted by primitives to ground truth using a variety of metrics; normals predicted by primitives to ground truth; and an oracle segmentation derived from primitives to ground truth segmentation. Depth metrics are: the (standard) AbsRel (eg [44]);  $AUC_n$ , which evaluates the fraction of points within  $n$  cm of the correct location (after [60, 28]); mean and median of the occlusion-aware distance of [28]. Normal metrics are based on [62] and are mean and median of angle to true normal, in degrees. The oracle segmentation metric uses an oracle to predict the best label for each image region, where regions consist of pixels with the same face intersection label (of Sec. 3), then compares this to ground truth. The SegAcc error metric shown in Tables 1 and 7 refers to the fraction of pixels labeled correctly. For LAION, we compute depth and normal metrics from generated primitives comparing to depth and normal predicted from the image.

| Dataset | faces | AbsRel↓ |
|---------|-------|---------|
| NYUv2   | 6     | 0.0417  |
| LAION   | 6     | 0.0193  |
| LAION   | 12    | 0.0178  |

Table 2: Depth metrics for NYUv2 data and LAION data compared, when ensembling pos + neg  $R \rightarrow S$ . The much larger data volume in LAION significantly improves the generalization ability of our procedure. Further, increasing the representational power of our method by removing the symmetric normal constraint (for parallelepipeds, top two rows) and increasing the number of faces per polytope to  $f = 12$  (bottom row) yields even better primitive decompositions.

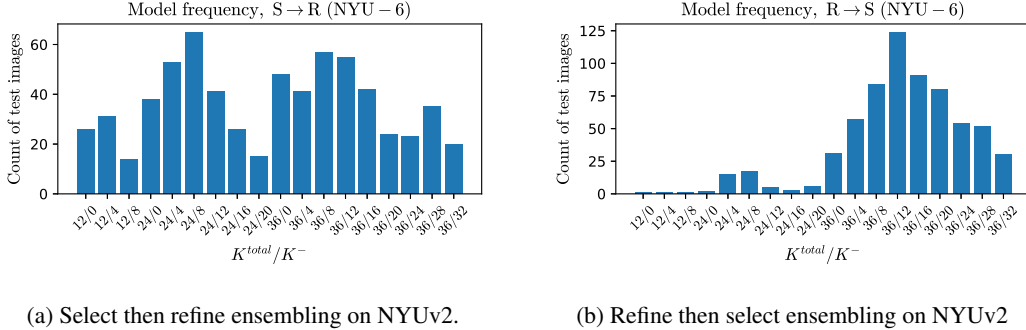


Figure 6: Boolean primitives are often selected from the ensemble. **Left** When we ensemble with  $S \rightarrow R$ , all models across all primitive counts are well-represented. This indicates that our network prediction may slightly struggle to manage larger numbers of primitives, hence the relative success of fewer primitives. In this setting, selecting a prediction for finetuning is based on fraction of 3D samples classified incorrectly, which is fast as we don’t need to finetune and render the outputs of all the networks to decide which model to use. **Right** When we refine then choose  $R \rightarrow S$ , our finetuning procedure polishes each network start point and chooses the best one based on AbsRel, requiring a render for each model. When doing so, the best model (measured by AbsRel of rendered depth against GT depth) is strongly concentrated among higher primitive counts,  $K^{total} = 36$ , though fewer primitives are still represented in the ensemble at times. Notice how the ensemble strongly favors representations with boolean primitives available, indicating they are useful in practice.

## 4.2 NYUv2 Results

**Our method beats SOTA** on depth, normal, and segmentation (Table 1). With or without ensembling process, **our method is faster than SOTA**. Qualitative results in Fig. 3. More extensive detailed comparison in Supplementary.

**Negative primitives make an important contribution**, as indicated by Fig. 6b. This figure shows the histogram of the number of times a particular  $(K^{total}, K^-)$  combination was selected. Note that there is a strong tendency to use more primitives ( $K^{total} = 36$  is much more popular than other options). One would expect this from bias considerations, but we observe that many scenes use fewer primitives. The number of negatives used for the best fit is quite variable, though often near  $K^- \approx \frac{1}{3}K^{total}$  - see Sec. B. We believe the ensembling step reduces variance by discarding complex fits that, while more flexible and thus lower in bias, tend to overfit and become less accurate. When these complex fits perform poorly, the ensemble instead favors simpler, more robust models.

**Our method is efficient**, as Table 3 shows. The vast majority of time is spent in polishing the representation. Ensembling yields further improvements (particularly  $S \rightarrow R$ ), and is still more efficient than prior work (see table 1).

## 4.3 LAION Results

Scaling is an important concept in computer vision, but we have not seen this concept applied to 3D primitive generation. To that end, we collect approx. 1.8M natural images from LAION-Aesthetic.



| $K^{total}$ | Encode | Loss   | Finetune | Render |
|-------------|--------|--------|----------|--------|
| <b>12</b>   | 0.0006 | 0.0006 | 0.68     | 0.15   |
| <b>24</b>   | 0.0006 | 0.0006 | 1.23     | 0.22   |
| <b>36</b>   | 0.0006 | 0.0007 | 1.79     | 0.26   |

Table 3: Estimated inference breakdown times, all times in seconds, 256-res images,  $K^- = 0$ . Encoding is very fast, in which the network predicts parameters of the primitives given an RGBD image. Computing loss, required for getting the fraction of samples classified correctly when ensembling with  $S \rightarrow R$ , is also fast. However, finetuning (we show 200 steps here) is often the bottleneck since we must compute the loss and optimize the parameters of the primitives. Since our primitives are the blended union of half-spaces [9], they cannot be rasterized easily and raymarching the SDF is required.

We use a recent SOTA depth estimation network [66] to obtain depth maps, and make reasonable camera calibration assumptions to lift a 3D point cloud from the depth map. In particular, we use the Hypersim [50] module that predicts metric depth and use its camera parameters to get the point cloud for each image, which is required for training our convex decomposition model. GT normals can be obtained using the image gradient method described in [60], which requires point cloud input. **LAION is easier than NYUv2** as Table 2 shows (note the improved AbsRel), likely due to the much larger dataset and availability of easier scenes. NYUv2 scenes are complex cluttered indoor rooms.

Our depth AbsRel numbers on LAION (comparing primitive depth against supplied depth map) lie between .019 to .029 (see Table 8). For reference, the state-of-the-art depth estimator DepthAnythingV2 [66] reports AbsRel values (predicted vs. ground truth depth) of approximately 0.044 to 0.075 on NYUv2 and KITTI, which helps contextualize that our depth errors are comparatively small.

**Our network start is much better than pure descent**, as Fig. 5 shows. The randomly started pure descent procedure of Section 3.2 produces surprisingly strong fits, but requires a large number of iterations to do so. Typically, 100 iterations of polishing a network start point is much better than 1000 iterations of pure descent. The descent procedure is a first order method, so we expect AbsRel to improve no faster than  $1/\text{iterations}$ , suggesting that this figure understates the advantage of the network start point.

## 5 Discussion

Primitives are an old obsession in computer vision. Their original purpose (object recognition) now appears to be much better handled in other ways. Mostly, using primitives was never really an issue, because there weren’t viable fitting procedures. But what are primitives for? Likely answers come from robotics – where one might benefit from simplified representations of geometry that are still accurate – and image editing – where a user might edit a scene by moving primitives (e.g. Fig. 7). Future work may better handle variable primitive representations (we train a separate network for each primitive count  $K^{total}/K^-$ ) and improve the network start, eliminating the need for post-training finetuning. While this paper has drastically advanced geometric accuracy of 3D primitive fitting to data, improving segmentation boundaries remains open.

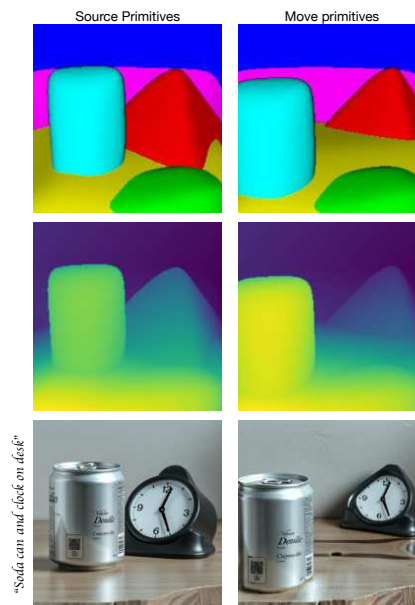


Figure 7: We show an example of extracting primitives from a scene (top left), and using its depth map (second row) to synthesize an image (bottom left). The second column shows primitive manipulations such that the newly synthesized image (bottom right) simultaneously respects the source texture and requested geometric positioning. Results from an in-submission follow-up work.

## References

- [1] Stephan Alaniz, Massimiliano Mancini, and Zeynep Akata. Iterative superquadric recomposition of 3d objects from multiple views. In *Proceedings of the IEEE/CVF International Conference on Computer Vision*, pages 18013–18023, 2023.
- [2] Barr. Superquadrics and angle-preserving transformations. *IEEE Computer Graphics and Applications*, 1:11–23, 1981.
- [3] Shariq Farooq Bhat, Niloy J. Mitra, and Peter Wonka. Loosecontrol: Lifting controlnet for generalized depth conditioning, 2023.
- [4] I Biederman. Recognition by components : A theory of human image understanding. *Psychological Review*, (94):115–147, 1987.
- [5] TO Binford. Visual perception by computer. In *IEEE Conf. on Systems and Controls*, 1971.
- [6] Stéphane Calderon and Tamy Boubekeur. Bounding proxies for shape approximation. *ACM Transactions on Graphics (TOG)*, 36:1 – 13, 2017.
- [7] Zhiqin Chen, Andrea Tagliasacchi, and Hao Zhang. Bsp-net: Generating compact meshes via binary space partitioning. *2020 IEEE/CVF Conference on Computer Vision and Pattern Recognition (CVPR)*, pages 42–51, 2019.
- [8] Boyang Deng, Simon Kornblith, and Geoffrey Hinton. Cerberus: A multi-headed derenderer. In *Workshop on 3D Scene Understanding*, 2019.
- [9] Boyang Deng, Kyle Genova, Soroosh Yazdani, Sofien Bouaziz, Geoffrey Hinton, and Andrea Tagliasacchi. Cvxnet: Learnable convex decomposition. June 2020.
- [10] M. A. Fischler and R. C. Bolles. Random sample consensus: A paradigm for model fitting with applications to image analysis and automated cartography. *Comm. ACM.*, 24(6):381–395, 1981.
- [11] David F. Fouhey, Abhinav Gupta, and Martial Hebert. Data-driven 3D primitives for single image understanding. In *ICCV*, 2013.
- [12] K. Fu, J. Peng, and Q. He et al. Single image 3d object reconstruction based on deep learning: A review. *Multimed Tools Appl*, 80:463–498, 2021.
- [13] Matheus Gadelha, Giorgio Gori, Duygu Ceylan, Radomír Mech, Nathan A. Carr, Tamy Boubekeur, Rui Wang, and Subhansu Maji. Learning generative models of shape handles. *2020 IEEE/CVF Conference on Computer Vision and Pattern Recognition (CVPR)*, pages 399–408, 2020.
- [14] Abhinav Gupta, Alexei A. Efros, and Martial Hebert. Blocks world revisited: Image understanding using qualitative geometry and mechanics. In *ECCV*, 2010.
- [15] Shreyas Hampali, Sinisa Stekovic, Sayan Deb Sarkar, Chetan Srinivasa Kumar, Friedrich Fraundorfer, and Vincent Lepetit. Monte carlo scene search for 3d scene understanding. *2021 IEEE/CVF Conference on Computer Vision and Pattern Recognition (CVPR)*, pages 13799–13808, 2021.
- [16] V. Hedau, D. Hoiem, and D. Forsyth. Recovering the Spatial Layout of Cluttered Rooms. In *Proc. ICCV*, 2009.
- [17] V. Hedau, D. Hoiem, and D. Forsyth. Recovering Free Space of Indoor Scenes from a Single Image. In *Proc. CVPR*, 2012.
- [18] Varsha Hedau, Derek Hoiem, and David Forsyth. Thinking Inside the Box: Using Appearance Models and Context Based on Room Geometry. In *Proc. ECCV*, 2010.
- [19] A. Hertz, O. Perel, O. Sorkine-Hornung, and D. Cohen-Or. Spaghetti: editing implicit shapes through part aware generation. *ACM Transactions on Graphics*, 41(4):1–20, 2022.
- [20] D. Hoiem, A. A. Efros, and M. Hebert. Recovering surface layout from an image. *IJCV*, 2007.

- [21] Derek Hoiem, Alexei A. Efros, and Martial Hebert. Automatic photo pop-up. *ACM Transactions on Graphics / SIGGRAPH*, 24(3), August 2005.
- [22] Aleš Jaklič, Aleš Leonardis, and Franc Solina. Segmentation and recovery of superquadrics. In *Computational Imaging and Vision*, 2000.
- [23] Eric Jang, Shixiang Gu, and Ben Poole. Categorical reparameterization with gumbel-softmax. In *International Conference on Learning Representations*, 2017. URL <https://openreview.net/forum?id=rkE3y85ee>.
- [24] Hao Jiang. Finding approximate convex shapes in rgb-d images. In *European Conference on Computer Vision*, pages 582–596. Springer, 2014.
- [25] Zhizhong Kang, Juntao Yang, Zhou Yang, and Sai Cheng. A review of techniques for 3d reconstruction of indoor environments. *ISPRS Int. J. Geo Inf.*, 9:330, 2020.
- [26] Florian Kluger and Bodo Rosenhahn. PARSAC: Accelerating Robust Multi-Model Fitting with Parallel Sample Consensus. In *AAAI*, 2024.
- [27] Florian Kluger, Eric Brachmann, Hanno Ackermann, Carsten Rother, Michael Ying Yang, and Bodo Rosenhahn. CONSAC: Robust Multi-Model Fitting by Conditional Sample Consensus. In *CVPR*, 2020.
- [28] Florian Kluger, Hanno Ackermann, Eric Brachmann, Michael Ying Yang, and Bodo Rosenhahn. Cuboids revisited: Learning robust 3d shape fitting to single rgb images. In *Proceedings of the IEEE Conference on Computer Vision and Pattern Recognition (CVPR)*, 2021.
- [29] Florian Kluger, Eric Brachmann, Michael Ying Yang, and Bodo Rosenhahn. Robust shape fitting for 3d scene abstraction. *IEEE Transactions on Pattern Analysis and Machine Intelligence*, 2024.
- [30] Lingxiao Li, Minhyuk Sung, Anastasia Dubrovina, L. Yi, and Leonidas J. Guibas. Supervised fitting of geometric primitives to 3d point clouds. *2019 IEEE/CVF Conference on Computer Vision and Pattern Recognition (CVPR)*, pages 2647–2655, 2018.
- [31] Chen Liu, Kihwan Kim, Jinwei Gu, Yasutaka Furukawa, and Jan Kautz. Planercnn: 3d plane detection and reconstruction from a single image. *2019 IEEE/CVF Conference on Computer Vision and Pattern Recognition (CVPR)*, pages 4445–4454, 2018.
- [32] Chen Liu, Jimei Yang, Duygu Ceylan, Ersin Yumer, and Yasutaka Furukawa. Planenet: Piece-wise planar reconstruction from a single rgb image. In *Proceedings of the IEEE Conference on Computer Vision and Pattern Recognition*, pages 2579–2588, 2018.
- [33] Haolin Liu, Yujian Zheng, Guanying Chen, Shuguang Cui, and Xiaoguang Han. Towards high-fidelity single-view holistic reconstruction of indoor scenes. In *European Conference on Computer Vision*, pages 429–446. Springer, 2022.
- [34] Ilya Loshchilov and Frank Hutter. Decoupled weight decay regularization, 2019. URL <https://arxiv.org/abs/1711.05101>.
- [35] D. Marr and H. K. Nishihara. Representation and recognition of the spatial organization of three-dimensional shapes. *Proceedings of the Royal Society of London. Series B. Biological Sciences*, 200(1140):269–294, 1978. ISSN 0080-4649. doi: 10.1098/rspb.1978.0020. URL <https://doi.org/10.1098/rspb.1978.0020>.
- [36] Kaichun Mo, Paul Guerrero, L. Yi, Hao Su, Peter Wonka, Niloy Jyoti Mitra, and Leonidas J. Guibas. Structurenets: Hierarchical graph networks for 3d shape generation. *ACM Trans. Graph.*, 38:242:1–242:19, 2019.
- [37] Tom Monnier, Jake Austin, Angjoo Kanazawa, Alexei Efros, and Mathieu Aubry. Differentiable blocks world: Qualitative 3d decomposition by rendering primitives. *Advances in Neural Information Processing Systems*, 36:5791–5807, 2023.
- [38] Pushmeet Kohli Nathan Silberman, Derek Hoiem and Rob Fergus. Indoor segmentation and support inference from rgb-d images. In *ECCV*, 2012.

- [39] R. Nevatia and T.O. Binford. Description and recognition of complex curved objects. *Artificial Intelligence*, 1977.
- [40] Despoina Paschalidou, Ali O. Ulusoy, and Andreas Geiger. Superquadrics revisited: Learning 3d shape parsing beyond cuboids. *2019 IEEE/CVF Conference on Computer Vision and Pattern Recognition (CVPR)*, pages 10336–10345, 2019.
- [41] Despoina Paschalidou, Angelos Katharopoulos, Andreas Geiger, and Sanja Fidler. Neural parts: Learning expressive 3d shape abstractions with invertible neural networks. In *CVPR*, 2021.
- [42] J. Ponce and M. Hebert. A new method for segmenting 3-d scenes into primitives. In *Proc. 6 ICPR*, 1982.
- [43] Michael Ramamonjisoa, Sinisa Stekovic, and Vincent Lepetit. Monteboxfinder: Detecting and filtering primitives to fit a noisy point cloud. *ArXiv*, abs/2207.14268, 2022.
- [44] René Ranftl, Katrin Lasinger, David Hafner, Konrad Schindler, and Vladlen Koltun. Towards robust monocular depth estimation: Mixing datasets for zero-shot cross-dataset transfer. *IEEE Transactions on Pattern Analysis and Machine Intelligence (TPAMI)*, 2020.
- [45] René Ranftl, Katrin Lasinger, David Hafner, Konrad Schindler, and Vladlen Koltun. Towards robust monocular depth estimation: Mixing datasets for zero-shot cross-dataset transfer. *IEEE Transactions on Pattern Analysis and Machine Intelligence*, 44(3), 2022.
- [46] A. A. G. Requicha. Mathematical models of rigid solid objects. In *Tech. Memo. No. 28, Production Automation Project, Univ. of Rochester*, 1977.
- [47] Aristides A. G. Requicha and Herbert B. Voelcker. Boolean operations in solid modeling: Boundary evaluation and merging algorithms. *Proceedings of the IEEE*, 73:30–44, 1985. URL <https://api.semanticscholar.org/CorpusID:17777160>.
- [48] Dominic Roberts, Aram Danielyan, Hang Chu, Mani Golparvar Fard, and David A. Forsyth. Lsd-structurenet: Modeling levels of structural detail in 3d part hierarchies. *2021 IEEE/CVF International Conference on Computer Vision (ICCV)*, pages 5816–5825, 2021.
- [49] L. G. Roberts. *Machine Perception of Three-Dimensional Solids*. PhD thesis, MIT, 1963.
- [50] Mike Roberts, Jason Ramapuram, Anurag Ranjan, Atulit Kumar, Miguel Angel Bautista, Nathan Paczan, Russ Webb, and Joshua M. Susskind. Hypersim: A photorealistic synthetic dataset for holistic indoor scene understanding, 2021. URL <https://arxiv.org/abs/2011.02523>.
- [51] S. Shafer and T. Kanade. The theory of straight homogeneous generalized cylinders. In *Technical Report CS-083-105, Carnegie Mellon University*, 1983.
- [52] Dmitriy Smirnov, Matthew Fisher, Vladimir G. Kim, Richard Zhang, and Justin M. Solomon. Deep parametric shape predictions using distance fields. *2020 IEEE/CVF Conference on Computer Vision and Pattern Recognition (CVPR)*, pages 558–567, 2019.
- [53] Sinisa Stekovic, Shreyas Hampali, Mahdi Rad, Sayan Deb Sarkar, Friedrich Fraundorfer, and Vincent Lepetit. General 3d room layout from a single view by render-and-compare. In *European Conference on Computer Vision*, pages 187–203. Springer, 2020.
- [54] Chun-Yu Sun and Qian-Fang Zou. Learning adaptive hierarchical cuboid abstractions of 3d shape collections. *ACM Transactions on Graphics (TOG)*, 38:1 – 13, 2019.
- [55] Maxim Tatarchenko, Stephan R. Richter, René Ranftl, Zhuwen Li, Vladlen Koltun, and Thomas Brox. What do single-view 3d reconstruction networks learn? *2019 IEEE/CVF Conference on Computer Vision and Pattern Recognition (CVPR)*, pages 3400–3409, 2019.
- [56] Maged S. Tawfik. An efficient algorithm for csg to b-rep conversion. In *Proceedings of the First ACM Symposium on Solid Modeling Foundations and CAD/CAM Applications, SMA '91*, page 99–108, New York, NY, USA, 1991. Association for Computing Machinery. ISBN 0897914279. doi: 10.1145/112515.112534. URL <https://doi.org/10.1145/112515.112534>.



- [57] Shubham Tulsiani, Hao Su, Leonidas J. Guibas, Alexei A. Efros, and Jitendra Malik. Learning shape abstractions by assembling volumetric primitives. In *Computer Vision and Pattern Recognition (CVPR)*, 2017.
- [58] Mikaela Angelina Uy, Yen-Yu Chang, Minhuk Sung, Purvi Goel, Joseph G Lambourne, Tolga Birdal, and Leonidas J Guibas. Point2cyl: Reverse engineering 3d objects from point clouds to extrusion cylinders. In *CVPR*, 2022.
- [59] A. van den Hengel, C. Russell, A. Dick, J. Bastian, L. Fleming D. Poo-ley, and L. Agapito. Part-based modelling of compound scenes from images. In *CVPR*, 2015.
- [60] Vaibhav Vavilala and David Forsyth. Convex decomposition of indoor scenes. In *Proceedings of the IEEE/CVF International Conference on Computer Vision (ICCV)*, pages 9176–9186, October 2023.
- [61] Vaibhav Vavilala, Seemantihar Jain, Rahul Vasanth, Anand Bhattad, and David Forsyth. Blocks2world: Controlling realistic scenes with editable primitives, 2023.
- [62] Xiaolong Wang, David Fouhey, and Abhinav Gupta. Designing deep networks for surface normal estimation. In *Proceedings of the IEEE conference on computer vision and pattern recognition*, pages 539–547, 2015.
- [63] X. Wei, M. Liu, Z. Ling, and H. Su. Approximate convex decomposition for 3d meshes with collision-aware concavity and tree search. *ACM Transactions on Graphics*, 41(4), 2022.
- [64] Rundi Wu, Chang Xiao, and Changxi Zheng. Deepcad: A deep generative network for computer-aided design models. In *ICCV*, 2021.
- [65] Lihe Yang, Bingyi Kang, Zilong Huang, Xiaogang Xu, Jiashi Feng, and Hengshuang Zhao. Depth anything: Unleashing the power of large-scale unlabeled data. In *CVPR*, 2024.
- [66] Lihe Yang, Bingyi Kang, Zilong Huang, Zhen Zhao, Xiaogang Xu, Jiashi Feng, and Hengshuang Zhao. Depth anything v2. *arXiv:2406.09414*, 2024.
- [67] Fenggen Yu, Zhiqin Chen, Manyi Li, Aditya Sanghi, Hooman Shayani, Ali Mahdavi-Amiri, and Hao Zhang. Capri-net: Learning compact cad shapes with adaptive primitive assembly. In *Proceedings of the IEEE/CVF Conference on Computer Vision and Pattern Recognition*, pages 11768–11778, 2022.
- [68] Chuhan Zou, Ersin Yumer, Jimei Yang, Duygu Ceylan, and Derek Hoiem. 3d-prnn: Generating shape primitives with recurrent neural networks. *2017 IEEE International Conference on Computer Vision (ICCV)*, pages 900–909, 2017.
- [69] Chuhan Zou, Ersin Yumer, Jimei Yang, Duygu Ceylan, and Derek Hoiem. 3d-prnn: Generating shape primitives with recurrent neural networks. In *Proceedings of the IEEE International Conference on Computer Vision (ICCV)*, Oct 2017.
- [70] Chuhan Zou, Alex Colburn, Qi Shan, and Derek Hoiem. Layoutnet: Reconstructing the 3d room layout from a single rgb image. In *Proceedings of the IEEE Conference on Computer Vision and Pattern Recognition (CVPR)*, June 2018.

## A Optimizing the Inference Pipeline

Given the computational cost of ensembling, we seek to maximize throughput of our inference pipeline. We use `torch.jit` and pure BFloat16 for encoding the RGBD image and finetuning. We also get speedups from batching the test images instead of one at a time. Combined with our subsampling strategy, these improvements yield over an order of magnitude faster inference than prior work, making ensembling more practical (see Table 1).

We note that rendering the primitives still requires FP32 precision to avoid unwanted artifacts. We accelerate our raymarcher by advancing the step size by  $0.8 \cdot \text{SDF}$  if it is greater than the minimum step size (we use 0.001 for large-scale metrics gathering, 0.0001 for beauty renders). We cannot advance by the full SDF because it is an approximation of how far the smoothed primitive boundary is. We apply interval halving at the intersection point to refine the estimate.

## B Boolean Primitives Theory

Set differencing can result in very efficient representations. Qualitative evidence was shown in Fig 2b, in which we model a cube with a hole punched in it. Intuitively, one positive and one negative primitive are sufficient to model it perfectly (2 total primitives). Without CSG, approx. 5 primitives may be required, which is less parameter-efficient. Based on that, we can sketch a theoretical argument as to why having a vocabulary of mixed positive and negative primitives is expected to yield more accurate representations than the same number of positive-only primitives.

### B.1 CSG Representational Efficiency

It is known that, for a CSG model in 3D with  $n$  distinct faces in the CSG tree, the resulting object model can have  $O(n^3)$  faces [56]. Relatively little appears to be known about the effect of the number of negative primitives on the complexity. We show that, under the circumstances that apply here, there are geometries that admit short descriptions using boolean primitives and have very much longer descriptions when only unions are allowed. The bound is obtained by reasoning about what is required to encode the area of an object.

For a shape  $S$ , let  $K_+(S)$  = minimum description length using only positive primitives and  $K_\pm(S)$  = minimum description length using mixed primitives. We claim that, under the circumstances that apply here, there are shapes such that  $K_\pm(S) \ll K_+(S)$ . The construction is straightforward.

**Preamble:** Primitives are smoothed polytopes as described in [9]. There is some (very large) finite bound on the number of faces. These primitives are convex by construction (so gaussian curvature is non-negative), but are smooth. The surface of these primitives consists of *flat* regions (where both normal and gaussian curvature are very close to zero), *edge* regions, where gaussian curvature is close to zero but normal curvature may be large, and *vertex* regions, where there is considerable gaussian curvature. These regions correspond to 2-faces, 1-faces and 0-faces in the underlying polytope. The actual values of the curvature are not significant for our purposes.

**Theorem 1.** *For the vocabulary of primitives described, there exist shapes  $S$  such that  $K_\pm(S) \ll K_+(S)$  when the representation of  $S$  is required to achieve sufficiently high precision.*

### Sketch of Proof

We construct a shape with this property. Write  $C$  for an approximation of a unit cube, represented as a smoothed polytope, and  $C'$  for that cube translated by  $(0.5, 0.5, 0.5)$ . Now consider  $S = C - C'$  (Figure 8). Clearly,  $K_\pm(S)$  is  $O(1)$ . Consider  $K_+(S)$  as the resolution  $\delta$  of the representation increases. Note from Figure 8 that representing  $S$  requires representing three concave edge-like regions, and one concave vertex-like region. Since we can use only positive primitives which are convex, we must use the flat faces. It is straightforward that representing the concave edge-like regions to resolution  $\delta$  will require  $O(1/\delta)$  flats, and representing the concave vertex-like region to resolution  $\delta$  will require  $O(1/\delta^2)$  flats. It follows that

$$\lim_{\delta \rightarrow 0} \frac{K_\pm}{K_+} = 0$$

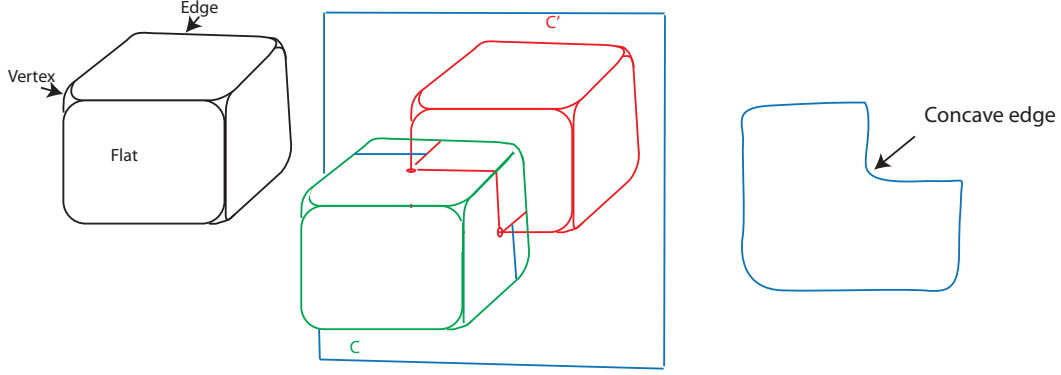


Figure 8: A shape which cannot be efficiently encoded as a union of convexes can be built out of a smoothed unit cube (on the **left**, showing *flat* regions, *edge* regions and *vertex* regions). **Center** sketches  $C$  (**green**) and  $C'$  (**red**), and a plane slicing the shape  $C - C'$  (**blue**). **Right** sketches the cross section cut by the plane: note the concave region, resulting from the smoothed convex edge region of  $C'$ . This requires at least  $O(1/\delta)$  convexes to approximate to precision  $\delta$ .

and so  $K_{\pm} \ll K_+$  in this case. Notice the underlying geometry of the effect is common – it takes a lot of convex shapes to represent concave cutouts. We expect that for “most shapes” the limit applies.

This theorem depends very delicately on the library of primitives and the transformations allowed to the primitives. In some cases, it is hopelessly *optimistic*. For example, if all primitives are cubes of two fixed sizes, where positives are large and negatives small, and transformations are purely Euclidean, it may not be possible to encode a set difference with positives only. We are not aware of bounds that take these effects into account.

## B.2 Optimal Ratio of Negative Primitives in CSG Modeling

A simple model leads to an intriguing result. For a fixed budget of primitives, we aim to determine the optimal ratio of negative primitives ( $K^-$ ) to positive primitives ( $K^+$ ) that maximizes representational efficiency.

A CSG model can be described as:

$$\text{Object} = (P_1 \cup P_2 \cup \dots \cup P_{K^+}) - (N_1 \cup N_2 \cup \dots \cup N_{K^-}) \quad (2)$$

Where  $P_i$  are positive primitives and  $N_j$  are negative primitives, with  $K^+ + K^- = K^{\text{total}}$ .

**Definitions:**

1. *Primitive Interaction*: Overlapping volumes creating representational complexity
2. *PP Interaction*: Between two positive primitives
3. *PN Interaction*: Between a positive and negative primitive

**Assumptions:**

1. Only positive volumes and their modifications by negative primitives are visible in the final result
2. The representational power comes primarily from *PP* and *PN* interactions
3. Primitives are distributed to maximize meaningful interactions
4. Optimal representation maximizes visible features per primitive used
5. Assume connected geometry

**Mathematical Model:**

1. Number of *PP* Interactions:  $\binom{K^+}{2} = \frac{K^+(K^+-1)}{2}$
2. Number of *PN* Interactions:  $K^+ \cdot K^-$

**Balancing *PP* and *PN* Interactions:**

For optimal efficiency, *PP* and *PN* interactions should be balanced:

$$\frac{K^+(K^+ - 1)}{2} \approx K^+ \cdot K^- \quad (3)$$

Substituting  $K^+ = K^{total} - K^-$  and simplifying:

$$\frac{(K^{total} - K^-)(K^{total} - K^- - 1)}{2} \approx (K^{total} - K^-) \cdot K^- \quad (4)$$

$$\frac{K^{total} - K^- - 1}{2} \approx K^- \quad (5)$$

For large  $K^{total}$ :

$$\frac{K^{total} - K^-}{2} \approx K^- \quad (6)$$

Solving:

$$K^{total} \approx 3K^- \quad (7)$$

$$\boxed{K^- \approx \frac{K^{total}}{3}} \quad (8)$$

Thus,

$$\boxed{K^+ \approx \frac{2K^{total}}{3}} \quad (9)$$

**Verification:** With this ratio, both interaction types equal approximately  $\frac{2(K^{total})^2}{9}$ , confirming our balance criterion.

**Empirical Evidence and Practical Verification:** This result is intriguing, because it is consistent with our experimental observations. It should be noted that the assumptions may not be sound (the losses on primitives should tend to lead to fewer interactions between positive primitives than our model requires), but experimental results suggest quite strongly that the best results are obtained when  $K^{total}/K^-$  is about 3. We believe this is likely some form of formal geometric property, rather than a coincidence. In our experimentation, all ratios of  $K^{total}/K^-$  provide excellent primitive representations, showing that our underlying neural network, losses, and data pipeline are sound. But on average, the *best* representations were near  $K^{total}/K^- \approx 3 : 1$ . Observe on both LAION and NYUv2 how depth and segmentation metrics tend to be best when  $K^{total}/K^-$  are near 36/12, 24/8, and 12/4 (Tables 7, 8, 9).

**Limitations from Overlap Loss:** The theoretical model balances *PP* interactions, representing the formation of the base positive volume, with *PN* interactions, representing the carving of details. While the introduction of a loss encouraging positive primitives to spread out and avoid overlap alters the nature of *PP* interactions—shifting them from forming dense, complex unions to defining a more distributed positive scaffold—the fundamental requirement for balancing these two generative forces remains. The term  $\binom{K^+}{2}$  can thus be interpreted as the capacity of positive primitives to establish this initial, potentially dispersed, positive volume. Our quantitative evaluations, performed under these conditions, confirm that the optimal ratio of approximately  $K^- \approx K^{total}/3$  persists. This empirical result suggests that the derived balance point robustly maximizes representational efficiency by ensuring sufficient primitives for both establishing the foundational positive elements of the scene and for subsequently sculpting them with negative primitives, aligning with principles of diminishing returns and complementary information.

### B.3 Face counts

In Sec. 3, we described how the number of faces scales with the number of boolean primitives. When computing segmentation accuracy with boolean primitives, we compute the triple  $(f_i, K_j^+, K_k^-)$  at each ray intersection point, where  $i$  is the face index,  $j$  is the index of the positive primitive we hit, and  $k$  is the index of the (potentially) negative primitive we hit. Each unique triple can get its own face label. Thus, given a fixed primitive budget  $K^{total}$ , replacing a pure positive primitive representation with a mixture of positives and negatives can yield more unique faces. For example,  $K^+/K^-$  maxes out at  $12f$  unique faces;  $K^+/K^-$  maxes out at  $42f$  faces. Note that  $f \times K^+ \times (1 + K^-)$  is the theoretical maximum of unique labels, as practical scenes do not involve every primitive touching every other primitive.

## C Primitives by Descent Alone

We generate a large reservoir of 1M free-space (a.k.a. bbx samples) for each test image. We still generate  $H \times W$  “inside” surface samples and “outside” surface samples near the depth boundary respectively, with  $\epsilon = 0.02$  units separating these surface samples. We remind the reader that our point clouds are renormalized to approx. the unit cube during training to avoid scale issues. Then during finetuning, we subsample from all available samples at each step, providing a rich gradient analogous to the network training process (though here, we’re optimizing the parameters of primitives). We found subsampling 10% of available samples sufficient at each step.

Second, we find that vanilla SGD does not produce usable results; instead AdamW [34] was required. We set the initial LR to 0.01, and linearly warm up to it over the first 25% of iterations. We then halve the learning rate once at 50% of the steps and again at 75%.

## D Additional Evaluation

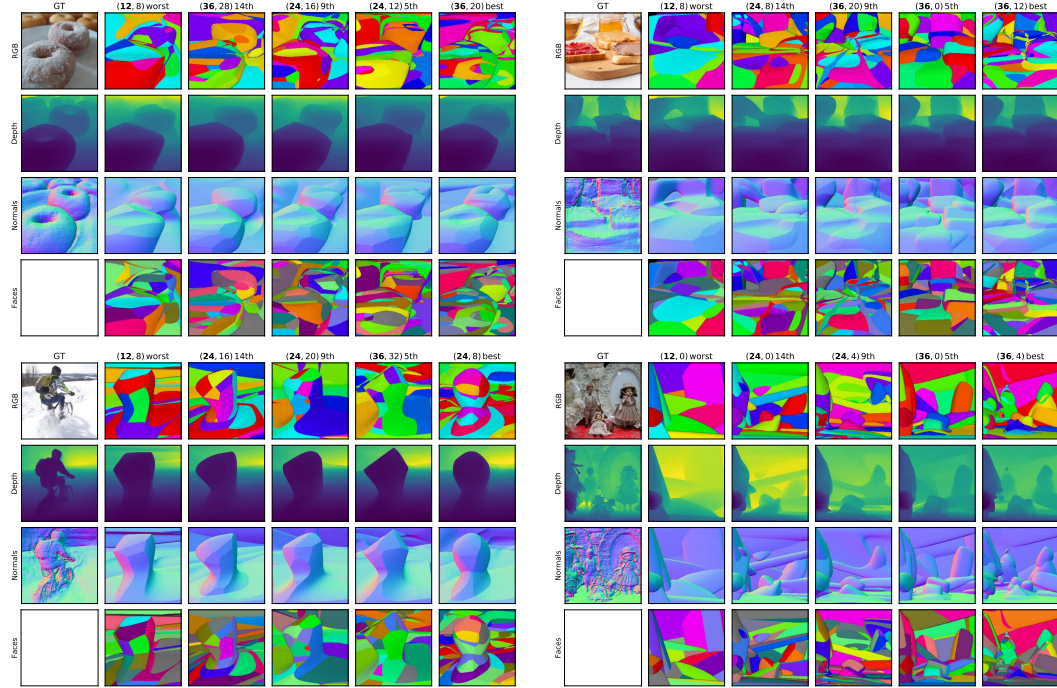


Figure 9: Additional qualitative examples shown.



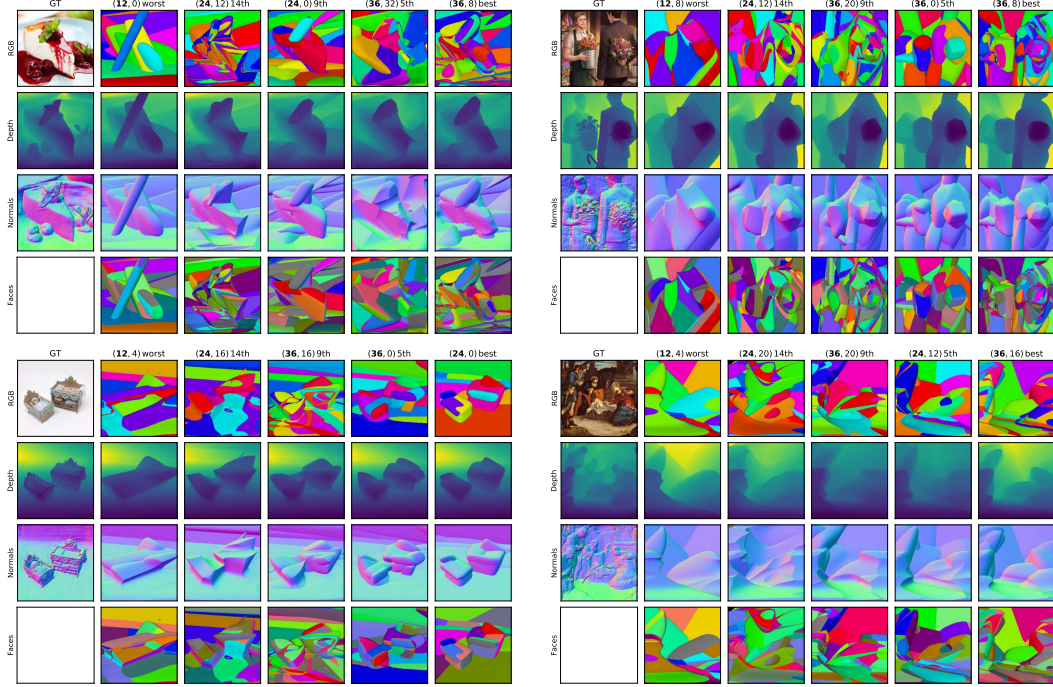
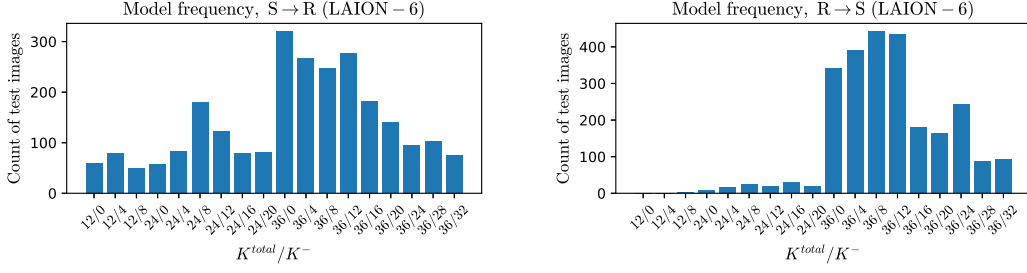


Figure 10: Additional qualitative examples shown.

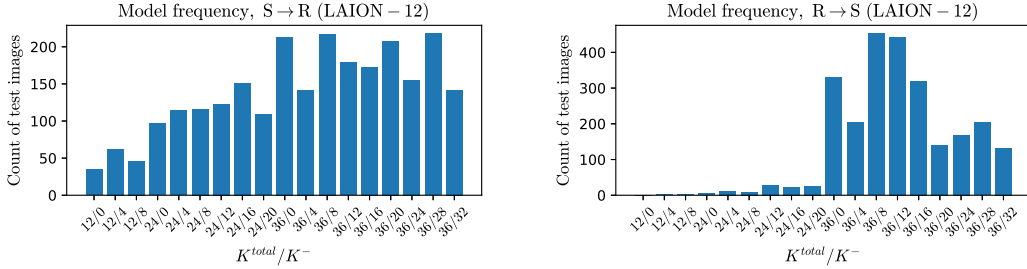
| Ensemble           | Refine            | $K^{total}$ | $K^-$ | $AUC_{@50} \uparrow$ | $AUC_{@20} \uparrow$ | $AUC_{@10} \uparrow$ | $AUC_{@5} \uparrow$ | $mean_{cm} \downarrow$ | $median_{cm} \downarrow$ |
|--------------------|-------------------|-------------|-------|----------------------|----------------------|----------------------|---------------------|------------------------|--------------------------|
| No                 | Yes               | 12          | 0     | 0.91                 | 0.827                | 0.725                | 0.572               | 0.186                  | 0.0507                   |
| No                 | Yes               | 12          | 4     | 0.917                | 0.84                 | 0.744                | 0.597               | 0.178                  | 0.045                    |
| No                 | Yes               | 12          | 8     | 0.908                | 0.821                | 0.717                | 0.568               | 0.195                  | 0.0523                   |
| No                 | Yes               | 24          | 0     | 0.928                | 0.862                | 0.777                | 0.634               | 0.154                  | 0.04                     |
| No                 | Yes               | 24          | 4     | 0.929                | 0.865                | 0.784                | 0.649               | 0.149                  | 0.0395                   |
| No                 | Yes               | 24          | 8     | 0.932                | 0.872                | 0.795                | 0.663               | 0.144                  | 0.0349                   |
| No                 | Yes               | 24          | 12    | 0.927                | 0.862                | 0.779                | 0.645               | 0.155                  | 0.0414                   |
| No                 | Yes               | 24          | 16    | 0.927                | 0.859                | 0.774                | 0.637               | 0.154                  | 0.0385                   |
| No                 | Yes               | 24          | 20    | 0.928                | 0.86                 | 0.773                | 0.632               | 0.154                  | 0.0392                   |
| No                 | Yes               | 36          | 0     | 0.934                | 0.876                | 0.799                | 0.664               | 0.141                  | 0.0358                   |
| No                 | Yes               | 36          | 4     | 0.935                | 0.878                | 0.806                | 0.677               | 0.138                  | 0.0335                   |
| No                 | Yes               | 36          | 8     | 0.934                | 0.879                | 0.807                | 0.681               | 0.139                  | 0.0351                   |
| No                 | Yes               | 36          | 12    | 0.936                | 0.882                | 0.812                | <b>0.69</b>         | 0.134                  | <b>0.0314</b>            |
| No                 | Yes               | 36          | 16    | 0.935                | 0.879                | 0.808                | 0.682               | 0.136                  | 0.0324                   |
| No                 | Yes               | 36          | 20    | 0.934                | 0.876                | 0.802                | 0.676               | 0.138                  | 0.0337                   |
| No                 | Yes               | 36          | 24    | 0.934                | 0.875                | 0.8                  | 0.671               | 0.139                  | 0.0337                   |
| No                 | Yes               | 36          | 28    | 0.934                | 0.875                | 0.8                  | 0.672               | 0.14                   | 0.0338                   |
| No                 | Yes               | 36          | 32    | 0.934                | 0.873                | 0.796                | 0.665               | 0.141                  | 0.0346                   |
| pos                | $S \rightarrow R$ | 26.1        | 0     | 0.926                | 0.86                 | 0.775                | 0.634               | 0.157                  | 0.0407                   |
| pos + neg          | $S \rightarrow R$ | 29          | 10.4  | 0.931                | 0.869                | 0.79                 | 0.658               | 0.147                  | 0.0363                   |
| pos                | $R \rightarrow S$ | 33.6        | 0     | 0.934                | 0.875                | 0.797                | 0.661               | 0.14                   | 0.0366                   |
| pos + neg          | $R \rightarrow S$ | 35          | 14.7  | <b>0.942</b>         | <b>0.887</b>         | <b>0.815</b>         | 0.689               | <b>0.125</b>           | 0.0319                   |
| No (Vavilala 2023) | Yes               | 13.9        | 0     | 0.869                | 0.725                | 0.565                | 0.382               | 0.266                  | 0.101                    |
| No (Kluger 2021)   | N/A               | -           | 0     | 0.772                | 0.627                | 0.491                | 0.343               | 0.208                  | -                        |

Table 4: **Baseline comparisons:** Ensembling strongly outperforms two recent SOTA methods, using the metrics reported by Kluger et al. [28], and using negative primitives in the ensemble produces further improvements. We show results with only positive primitives present pos, three networks,  $K^{total} \in \{12, 24, 36\}$ , as well as with positive and negative primitives pos + neg, 18 networks,  $K^- \in \{0, 4, \dots, K^{total} - 4\}$ . Our ensembles significantly outperform existing work. Further, we present results on the 18 methods we trained, where  $K^{total}/K^-$  is shown. Even without ensembling, any individual method we trained performs better than the baselines. Notice that boolean primitives are helpful on average.



(a) Select then refine ensembling on LAION 6 faces. (b) Refine then select ensembling on LAION 6 faces

Figure 11: Distribution of models chosen on LAION (6 faces), 2500 image test set. Models with boolean primitives are often chosen, especially after finetuning.



(a) Select then refine ensembling on LAION 12 faces. (b) Refine then select ensembling on LAION 12 faces

Figure 12: Distribution of models chosen on LAION (12 faces), 2500 image test set. Models with boolean primitives are often chosen, especially after finetuning.

| Ensemble  | Refine            | $K^{total}$ | $K^-$ | AUC <sub>@50</sub> ↑ | AUC <sub>@20</sub> ↑ | AUC <sub>@10</sub> ↑ | AUC <sub>@5</sub> ↑ | mean <sub>cm</sub> ↓ | median <sub>cm</sub> ↓ |
|-----------|-------------------|-------------|-------|----------------------|----------------------|----------------------|---------------------|----------------------|------------------------|
| No        | Yes               | 12          | 0     | 0.953                | 0.904                | 0.841                | 0.75                | 0.128                | 0.0364                 |
| No        | Yes               | 12          | 4     | 0.953                | 0.905                | 0.844                | 0.755               | 0.127                | 0.0345                 |
| No        | Yes               | 12          | 8     | 0.954                | 0.905                | 0.842                | 0.75                | 0.125                | 0.037                  |
| No        | Yes               | 24          | 0     | 0.963                | 0.924                | 0.87                 | 0.79                | 0.104                | 0.0288                 |
| No        | Yes               | 24          | 4     | 0.964                | 0.925                | 0.873                | 0.793               | 0.101                | 0.0276                 |
| No        | Yes               | 24          | 8     | 0.964                | 0.926                | 0.876                | 0.798               | 0.101                | 0.0267                 |
| No        | Yes               | 24          | 12    | 0.963                | 0.923                | 0.87                 | 0.791               | 0.104                | 0.0302                 |
| No        | Yes               | 24          | 16    | 0.964                | 0.923                | 0.87                 | 0.788               | 0.101                | 0.0287                 |
| No        | Yes               | 24          | 20    | 0.963                | 0.921                | 0.867                | 0.785               | 0.104                | 0.0293                 |
| No        | Yes               | 36          | 0     | 0.967                | 0.932                | 0.883                | 0.807               | 0.0965               | 0.0257                 |
| No        | Yes               | 36          | 4     | 0.967                | 0.933                | 0.886                | 0.811               | 0.0974               | 0.0272                 |
| No        | Yes               | 36          | 8     | 0.968                | 0.934                | 0.887                | 0.813               | 0.0921               | <b>0.024</b>           |
| No        | Yes               | 36          | 12    | 0.967                | 0.933                | 0.886                | 0.813               | 0.0929               | 0.0242                 |
| No        | Yes               | 36          | 16    | 0.967                | 0.931                | 0.882                | 0.806               | 0.0932               | 0.0256                 |
| No        | Yes               | 36          | 20    | 0.966                | 0.929                | 0.879                | 0.802               | 0.0956               | 0.0272                 |
| No        | Yes               | 36          | 24    | 0.967                | 0.93                 | 0.879                | 0.802               | 0.0928               | 0.0263                 |
| No        | Yes               | 36          | 28    | 0.963                | 0.924                | 0.872                | 0.793               | 0.104                | 0.0365                 |
| No        | Yes               | 36          | 32    | 0.962                | 0.923                | 0.871                | 0.793               | 0.106                | 0.0357                 |
| pos       | $S \rightarrow R$ | 30.3        | 0     | 0.963                | 0.925                | 0.872                | 0.794               | 0.104                | 0.0286                 |
| pos + neg | $S \rightarrow R$ | 31.3        | 10.6  | 0.965                | 0.927                | 0.877                | 0.8                 | 0.0985               | 0.0273                 |
| pos       | $R \rightarrow S$ | 34.4        | 0     | 0.967                | 0.932                | 0.882                | 0.805               | 0.0949               | 0.0262                 |
| pos + neg | $R \rightarrow S$ | 35.4        | 11.7  | <b>0.971</b>         | <b>0.937</b>         | <b>0.889</b>         | <b>0.814</b>        | <b>0.0827</b>        | 0.0244                 |

Table 5: **Quantitative evaluation on LAION 6 face polytopes:** We train and ensemble models on a subset of LAION, with approx. 1.8M images in the training set and 2500 in the test set. We report error metrics defined in by Kluger et al. [28]. Negative primitives remain useful, noting the italicized error metrics in each block of  $K^{total}$  always has boolean primitives. Ensembling produces further improvements similar to NYUv2. Our method scales very well to in-the-wild scenes, producing even better metrics than NYUv2 given the larger dataset.

| Ensemble  | Refine            | $K^{total}$ | $K^-$ | AUC@50 $\uparrow$ | AUC@20 $\uparrow$ | AUC@10 $\uparrow$ | AUC@5 $\uparrow$ | mean <sub>cm</sub> $\downarrow$ | median <sub>cm</sub> $\downarrow$ |
|-----------|-------------------|-------------|-------|-------------------|-------------------|-------------------|------------------|---------------------------------|-----------------------------------|
| No        | Yes               | <b>12</b>   | 0     | 0.959             | 0.913             | 0.854             | 0.765            | 0.114                           | 0.0339                            |
| No        | Yes               | <b>12</b>   | 4     | 0.96              | 0.918             | 0.863             | 0.779            | 0.108                           | 0.0299                            |
| No        | Yes               | <b>12</b>   | 8     | 0.961             | 0.918             | 0.862             | 0.777            | 0.108                           | 0.0301                            |
| No        | Yes               | <b>24</b>   | 0     | 0.967             | 0.931             | 0.881             | 0.804            | 0.0959                          | 0.0268                            |
| No        | Yes               | <b>24</b>   | 4     | 0.968             | 0.934             | 0.885             | 0.81             | 0.0912                          | 0.0248                            |
| No        | Yes               | <b>24</b>   | 8     | 0.968             | 0.933             | 0.885             | 0.811            | 0.0916                          | 0.0246                            |
| No        | Yes               | <b>24</b>   | 12    | 0.969             | 0.935             | 0.887             | 0.812            | 0.0881                          | 0.0243                            |
| No        | Yes               | <b>24</b>   | 16    | 0.968             | 0.934             | 0.886             | 0.812            | 0.0898                          | 0.0243                            |
| No        | Yes               | <b>24</b>   | 20    | 0.967             | 0.928             | 0.877             | 0.801            | 0.0927                          | 0.0274                            |
| No        | Yes               | <b>36</b>   | 0     | 0.97              | 0.939             | 0.893             | 0.821            | 0.0872                          | 0.0236                            |
| No        | Yes               | <b>36</b>   | 4     | 0.971             | 0.94              | 0.895             | 0.823            | 0.0841                          | 0.0227                            |
| No        | Yes               | <b>36</b>   | 8     | 0.971             | 0.941             | 0.897             | 0.827            | 0.0829                          | 0.0218                            |
| No        | Yes               | <b>36</b>   | 12    | 0.972             | 0.942             | 0.898             | 0.828            | 0.0816                          | <b>0.0217</b>                     |
| No        | Yes               | <b>36</b>   | 16    | 0.971             | 0.94              | 0.896             | 0.825            | 0.0837                          | 0.0221                            |
| No        | Yes               | <b>36</b>   | 20    | 0.971             | 0.939             | 0.892             | 0.82             | 0.0845                          | 0.0231                            |
| No        | Yes               | <b>36</b>   | 24    | 0.971             | 0.939             | 0.894             | 0.822            | 0.0836                          | 0.0227                            |
| No        | Yes               | <b>36</b>   | 28    | 0.971             | 0.939             | 0.892             | 0.819            | 0.084                           | 0.0232                            |
| No        | Yes               | <b>36</b>   | 32    | 0.971             | 0.938             | 0.891             | 0.818            | 0.0851                          | 0.0234                            |
| pos       | $S \rightarrow R$ | <b>29.8</b> | 0     | 0.967             | 0.933             | 0.884             | 0.808            | 0.0943                          | 0.0262                            |
| pos + neg | $S \rightarrow R$ | <b>31.2</b> | 13.5  | 0.969             | 0.935             | 0.888             | 0.815            | 0.0884                          | 0.0245                            |
| pos       | $R \rightarrow S$ | <b>35.3</b> | 0     | 0.97              | 0.938             | 0.892             | 0.82             | 0.0867                          | 0.0241                            |
| pos + neg | $R \rightarrow S$ | <b>35.5</b> | 13.2  | <b>0.974</b>      | <b>0.944</b>      | <b>0.899</b>      | <b>0.829</b>     | <b>0.0759</b>                   | 0.022                             |

Table 6: **Quantitative evaluation on LAION 12 face polytopes:** Most recent literature on primitive-fitting focuses on cuboids or parallelepipeds, but our model is capable of fitting polytopes of variable face count. All error metrics get better with more faces, which indicates more complex primitives yield more accurate representations.

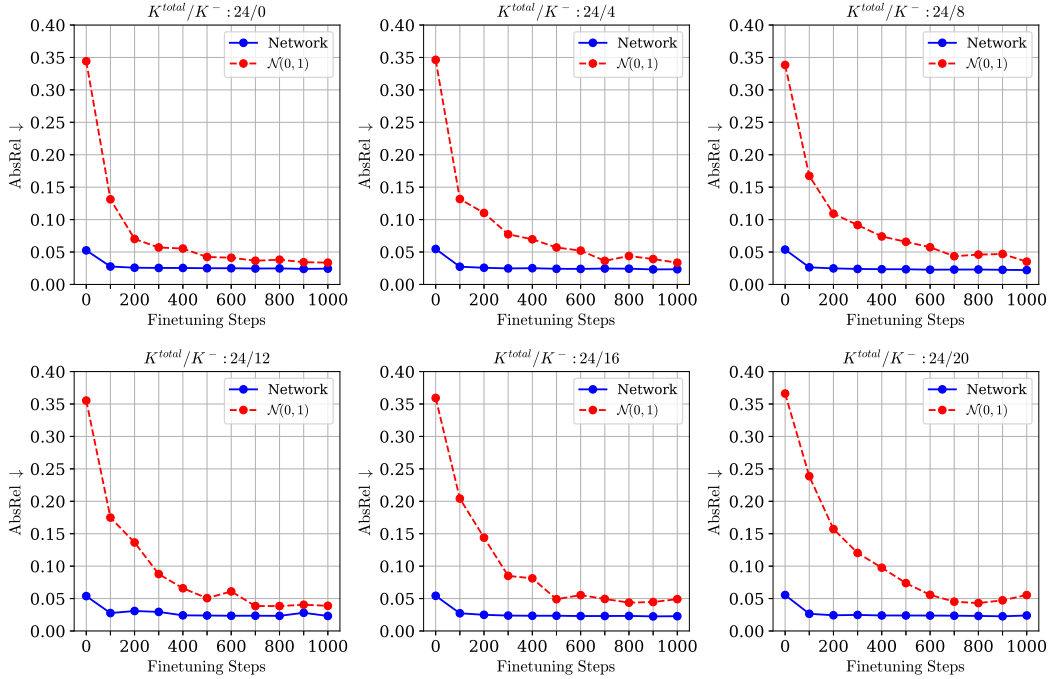


Figure 13: Additional examples on the value of network start, on 100 LAION test images,  $K^{total} = 24$ .

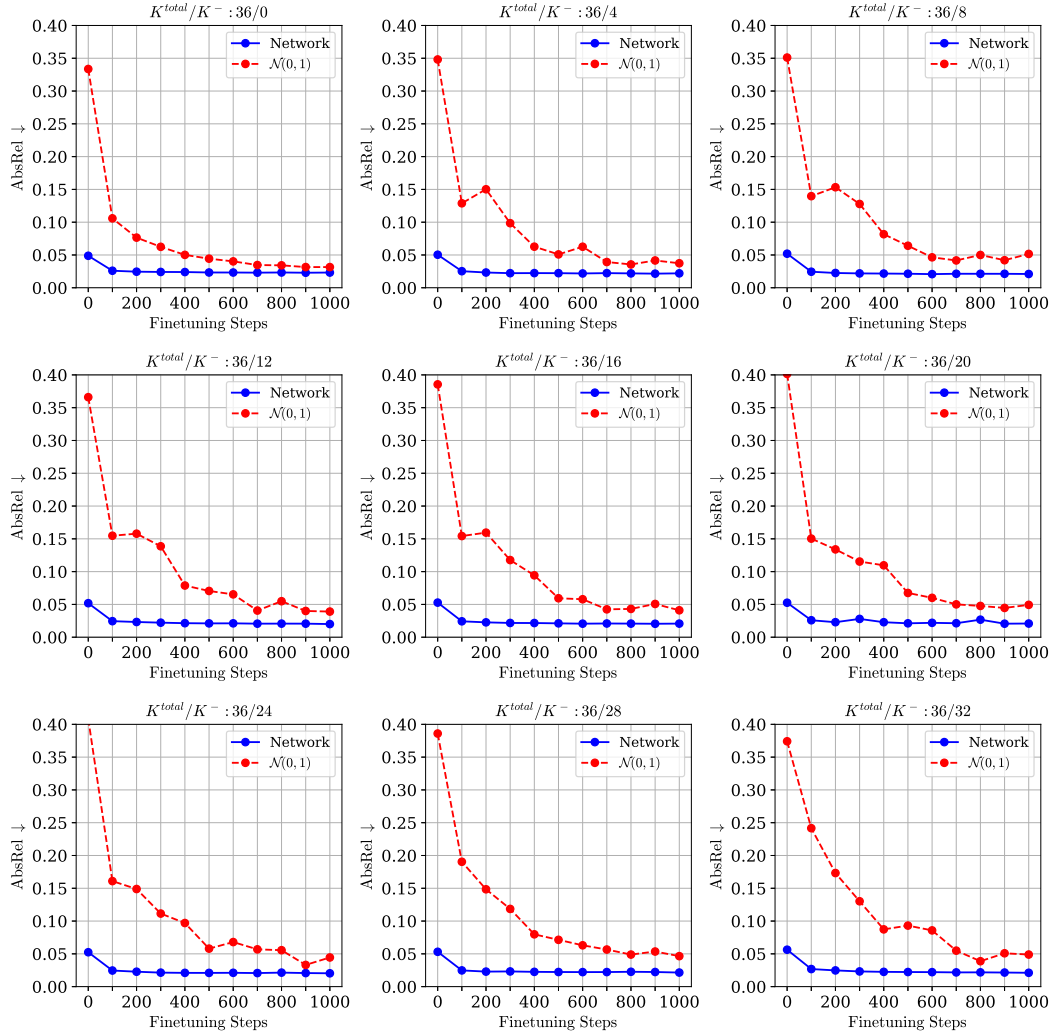


Figure 14: Additional examples on the value of network start, on 100 LAION test images,  $K^{total} = 36$ .

| Ensemble                    | $K^{total}$ | $K^-$ | AbsRel↓       | Normals Mean↓ | Normals Median↓ | SegAcc↑      |
|-----------------------------|-------------|-------|---------------|---------------|-----------------|--------------|
| No                          | <b>12</b>   | 0     | 0.0622        | 34.4          | 26.3            | 0.651        |
| No                          | <b>12</b>   | 4     | 0.0597        | 34.5          | 26.3            | 0.68         |
| No                          | <b>12</b>   | 8     | 0.064         | 35.7          | 27.2            | 0.666        |
| <hr/>                       |             |       |               |               |                 |              |
| No                          | <b>24</b>   | 0     | 0.052         | 33            | 25              | 0.7          |
| No                          | <b>24</b>   | 4     | 0.0504        | 33            | 24.9            | 0.726        |
| No                          | <b>24</b>   | 8     | 0.0486        | 32.7          | 24.6            | 0.742        |
| No                          | <b>24</b>   | 12    | 0.0514        | 33.4          | 25.3            | 0.724        |
| No                          | <b>24</b>   | 16    | 0.0506        | 33.8          | 25.7            | 0.724        |
| No                          | <b>24</b>   | 20    | 0.0508        | 33.9          | 25.6            | 0.709        |
| <hr/>                       |             |       |               |               |                 |              |
| No                          | <b>36</b>   | 0     | 0.0484        | 32.3          | 24.4            | 0.723        |
| No                          | <b>36</b>   | 4     | 0.0467        | 32.3          | 24.3            | 0.752        |
| No                          | <b>36</b>   | 8     | 0.0469        | 32.2          | 24.2            | 0.757        |
| No                          | <b>36</b>   | 12    | 0.0452        | 32.1          | 24              | <b>0.765</b> |
| No                          | <b>36</b>   | 16    | 0.0462        | 32.3          | 24.3            | 0.756        |
| No                          | <b>36</b>   | 20    | 0.0463        | 32.6          | 24.5            | 0.756        |
| No                          | <b>36</b>   | 24    | 0.0464        | 32.8          | 24.6            | 0.748        |
| No                          | <b>36</b>   | 28    | 0.0466        | 32.8          | 24.7            | 0.745        |
| No                          | <b>36</b>   | 32    | 0.047         | 33            | 24.8            | 0.735        |
| <hr/>                       |             |       |               |               |                 |              |
| pos $S \rightarrow R$       | <b>26.1</b> | 0     | 0.0527        | 33            | 24.9            | 0.7          |
| pos + neg $S \rightarrow R$ | <b>29</b>   | 10.4  | 0.0492        | 32.9          | 24.7            | 0.733        |
| pos $R \rightarrow S$       | <b>33.6</b> | 0     | 0.0476        | 32.3          | 24.4            | 0.72         |
| pos + neg $R \rightarrow S$ | <b>35</b>   | 14.7  | <b>0.0417</b> | <b>31.9</b>   | <b>24</b>       | 0.756        |
| <hr/>                       |             |       |               |               |                 |              |
| Vavilala & Forsyth [60]     | <b>13.9</b> | 0     | 0.098         | 37.4          | 32.4            | 0.618        |

Table 7: **Detailed error metrics on NYUv2.**

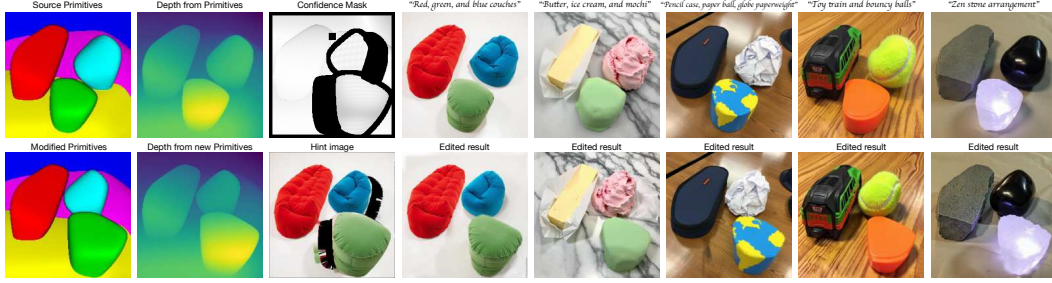
| Ensemble                    | $K^{total}$ | $K^-$ | AbsRel↓       | Normals Mean↓ | Normals Median↓ | $Neg\_per\_pos$ |
|-----------------------------|-------------|-------|---------------|---------------|-----------------|-----------------|
| No                          | <b>12</b>   | 0     | 0.0297        | 35.6          | 29.3            | 0               |
| No                          | <b>12</b>   | 4     | 0.0295        | 35.6          | 29.1            | 1.42            |
| No                          | <b>12</b>   | 8     | 0.029         | 35.8          | 29.2            | 4.13            |
| <hr/>                       |             |       |               |               |                 |                 |
| No                          | <b>24</b>   | 0     | 0.0244        | 33.9          | 27.5            | 0               |
| No                          | <b>24</b>   | 4     | 0.0238        | 33.9          | 27.4            | 0.719           |
| No                          | <b>24</b>   | 8     | 0.0235        | 33.7          | 27              | 1.54            |
| No                          | <b>24</b>   | 12    | 0.0242        | 34            | 27.4            | 2.39            |
| No                          | <b>24</b>   | 16    | 0.0235        | 34            | 27.4            | 3.94            |
| No                          | <b>24</b>   | 20    | 0.0242        | 34.2          | 27.5            | 8.04            |
| <hr/>                       |             |       |               |               |                 |                 |
| No                          | <b>36</b>   | 0     | 0.0225        | 33            | 26.7            | 0               |
| No                          | <b>36</b>   | 4     | 0.0223        | 32.9          | 26.4            | 0.548           |
| No                          | <b>36</b>   | 8     | 0.0217        | 32.9          | 26.3            | 1.01            |
| No                          | <b>36</b>   | 12    | 0.0218        | 32.9          | 26.3            | 1.5             |
| No                          | <b>36</b>   | 16    | 0.0217        | 33.2          | 26.6            | 1.9             |
| No                          | <b>36</b>   | 20    | 0.0221        | 33.4          | 26.8            | 2.55            |
| No                          | <b>36</b>   | 24    | 0.0215        | 33.3          | 26.7            | 3.81            |
| No                          | <b>36</b>   | 28    | 0.0236        | 33.8          | 27.1            | 5.49            |
| No                          | <b>36</b>   | 32    | 0.0243        | 33.9          | 27.3            | 10.8            |
| <hr/>                       |             |       |               |               |                 |                 |
| pos $S \rightarrow R$       | <b>30.3</b> | 0     | 0.0242        | 33.6          | 27.2            | 0               |
| pos + neg $S \rightarrow R$ | <b>31.3</b> | 10.6  | 0.0229        | 33.4          | 26.8            | 2.04            |
| pos $R \rightarrow S$       | <b>34.4</b> | 0     | 0.0221        | 33.1          | 26.7            | 0               |
| pos + neg $R \rightarrow S$ | <b>35.4</b> | 11.7  | <b>0.0193</b> | <b>32.7</b>   | <b>26.2</b>     | 1.94            |

Table 8: **Additional error metrics on LAION, 6 faces. The final column,  $Neg\_per\_pos$ , evaluates the average number of negative primitives touching each positive primitive, quantitatively showing negative primitives active in the geometric abstraction.**

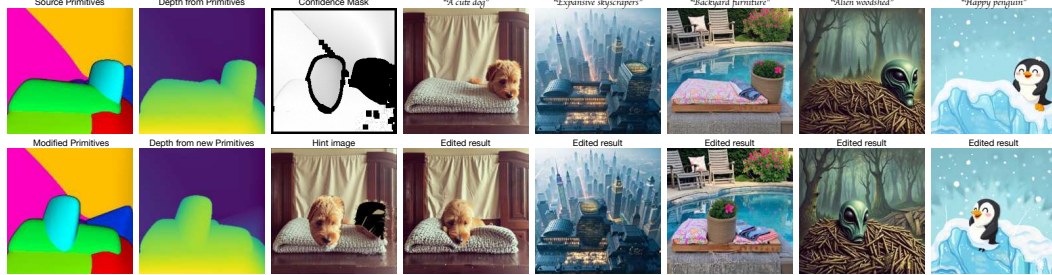


| Ensemble                    | $K^{total}$ | $K^-$ | AbsRel↓       | Normals Mean↓ | Normals Median↓ | $Neg\_per\_pos$ |
|-----------------------------|-------------|-------|---------------|---------------|-----------------|-----------------|
| No                          | <b>12</b>   | 0     | 0.0265        | 34.8          | 28.4            | 0               |
| No                          | <b>12</b>   | 4     | 0.0253        | 34.3          | 27.8            | 1.35            |
| No                          | <b>12</b>   | 8     | 0.0252        | 34.4          | 27.8            | 3.89            |
| No                          | <b>24</b>   | 0     | 0.0223        | 33.1          | 26.6            | 0               |
| No                          | <b>24</b>   | 4     | 0.0215        | 32.9          | 26.2            | 0.832           |
| No                          | <b>24</b>   | 8     | 0.0216        | 32.8          | 26.2            | 1.49            |
| No                          | <b>24</b>   | 12    | 0.0208        | 32.7          | 26.1            | 2.48            |
| No                          | <b>24</b>   | 16    | 0.021         | 32.8          | 26.1            | 4.04            |
| No                          | <b>24</b>   | 20    | 0.0222        | 33.3          | 26.6            | 7.64            |
| No                          | <b>36</b>   | 0     | 0.0203        | 32.2          | 25.7            | 0               |
| No                          | <b>36</b>   | 4     | 0.0199        | 32.2          | 25.6            | 0.648           |
| No                          | <b>36</b>   | 8     | 0.0196        | 32            | 25.3            | 1.1             |
| No                          | <b>36</b>   | 12    | 0.0193        | 32            | 25.3            | 1.59            |
| No                          | <b>36</b>   | 16    | 0.0198        | 32.1          | 25.4            | 2.11            |
| No                          | <b>36</b>   | 20    | 0.0199        | 32.3          | 25.6            | 2.76            |
| No                          | <b>36</b>   | 24    | 0.0197        | 32.2          | 25.6            | 3.88            |
| No                          | <b>36</b>   | 28    | 0.0198        | 32.3          | 25.6            | 6.17            |
| No                          | <b>36</b>   | 32    | 0.0201        | 32.4          | 25.7            | 10.9            |
| pos $S \rightarrow R$       | <b>29.8</b> | 0     | 0.0218        | 32.7          | 26.3            | 0               |
| pos + neg $S \rightarrow R$ | <b>31.2</b> | 13.5  | 0.0207        | 32.5          | 25.9            | 2.93            |
| pos $R \rightarrow S$       | <b>35.3</b> | 0     | 0.0201        | 32.2          | 25.8            | 0               |
| pos + neg $R \rightarrow S$ | <b>35.5</b> | 13.2  | <b>0.0178</b> | <b>31.8</b>   | <b>25.2</b>     | 2.53            |

Table 9: **Additional error metrics on LAION, 12 faces. The final column,  $Neg\_per\_pos$ , evaluates the average number of negative primitives touching each positive primitive, quantitatively showing negative primitives active in the geometric abstraction.**



(a)  $K = 6$  parts.



(b)  $K = 8$  parts.

Figure 15: We show results from an in-submission follow-up work. Applying the same primitive edit for different text prompts at coarse scale ( $K \in \{6, 8\}$  parts). The first row in each subplot contains source primitives and depth (first two columns); the confidence mask for hint generation; followed by five source RGB images. The second row shows the modified primitives and depth, followed by the hint image  $x_{hint}$ , followed by the five corresponding edited images. At coarse scales, moving a primitive can move a lot of texture at once. Observe how our hint generation procedure automatically yields confidence masks and hints, assigning low confidence to boundaries of primitives that moved (e.g. the dog’s hair) and revealed holes when moving objects. The diffusion model cleans up the low confidence regions and even handles blurry/aliased texture in the hint when  $t_{end} > 0$ , meaning that the hint is not used for some denoising steps.

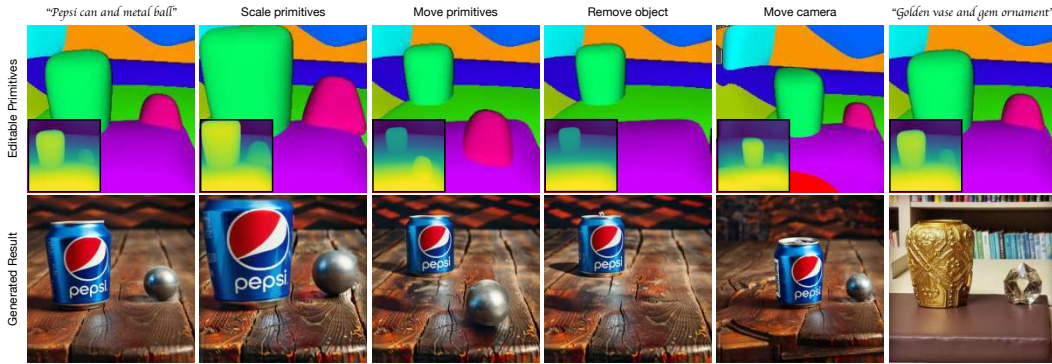


Figure 16: **Our method can decompose natural images into primitives, and be used to condition controlled image synthesis tasks.** We show results from an in-submission follow-up work, which uses a convex decomposition method similar to the one described here. The first row shows controlling primitives, the second shows synthesized results. The first column shows an initial set of primitives and RGB image; subsequent columns show various sequential edits such as scaling primitives, translation in 3D space, removing an object, moving the camera, and finally - changing the text caption.